Assembly of two new hybrid chloride materials with potential NLO properties: Structure elucidation, empirical and computational studies

Ikram Jomaa, Noureddine Issaoui, Thierry Roisnel, Houda Marouani

Assembly of two new hybrid chloride materials with potential NLO properties: Structure elucidation, empirical and computational studies

Ikram Jomaa [a], Noureddine Issaoui [b], Thierry Roisnel [c] and Houda Marouani [a,*]

[a] Université de Carthage, Faculté des Sciences de Bizerte, LR13ES08 Laboratoire de Chimie des Matériaux, 7021, Bizerte, Tunisie

[b] University of Monastir, Laboratory of Quantum and Statistical Physics LR18ES18, Faculty of Sciences, Monastir 5079, Tunisia

[c] Univ Rennes, CNRS, ISCR (Institut des Sciences Chimiques de Rennes) – UMR 6226, F-35000 Rennes, France

*Correspondence e-mail: houdamarouani2015@gmail.com

Abstract

This paper deals with the crystal structure of two new non-centrosymmetric hybrid compounds obtained from an aqueous solution by slow evaporation method and characterized by various techniques mainly single-crystal X-ray diffraction. In the atomic arrangement of 2-methylbenzylammonium chloride (1) the organic cations and the chloride anions are linked to each other via N-H…Cl hydrogen bonds, organic cations in zigzag distribution along b-axis in z = 0 and z = ½, are also close enough to enable a C–H…π interaction to occur. In 3-methylbenzylammonium chloride (2), the organic cations are linked together by C-H…π interactions and through N-H…Cl and C-H…Cl hydrogen bonds to form a two-dimensional network. To support experimental results, DFT calculations have been accomplished via the B3LYP method and 6-311++G(d,p) basis set on molecular geometry, vibrational and electronic properties. The non-covalent interactions were studied quantitatively using the Hirshfeld surfaces (HS) associated with 2D fingerprint plots. The NLO properties have been also investigated by DFT and compared to the urea reference.

Keywords: 2-methylbenzylamine; 3-methylbenzylamine; X-ray diffraction; Hirshfeld surface; DFT calculations; NLO.

1. Introduction

Designing new solids with specific properties was the main goal behind combining organic and inorganic materials. The tremendous possibilities of mixing the different properties offered by individual organic/inorganic counterparts open up a wide field of application **[1-9]**, they are also of growing interest due to their variable frameworks, and their potential photoluminescent and nonlinear optical (NLO) properties since this assembly is a way to give noncentrosymmetric crystal structures producing nonlinear optical materials.

Nonlinear Optical Crystals (NLOs) have received great concern, due to their potential applications in telecommunications, optical storage, optical parametric amplification, optical image processing, laser fusion reaction, photonics, laser remote sensing, medical diagnostics, etc. **[10-13]**. In general, organic crystals exhibit better nonlinear optical efficiency, but they tend to be less efficient in terms of physical and mechanical properties, here the inorganic counterpart compensates for these drawbacks.

Among these materials, Benzylamine and its derivatives that act as good inhibitors for proteolytic enzymes, such as trypsin, plasmin, and thrombin **[14-16],** tend to give noncentrosymmetric crystal structures namely, 3-methylbenzylammonium trioxonitrate **[17],** Bis(4-methylbenzylammonium) tetrabromidozincate **[18],** and bis(4-methylbenzylammonium) tetrachloridocadmate(II) **[19].** Else, halide anions have been successfully used to assemble various molecules containing aromatic groups, with C-H…π stacking interactions within the matrix. These anions can be useful for such applications because of the high flexibility of their coordination **[20-23].**

In the present study, the foremost idea is to show the occurrence and nature of weak noncovalent interactions in the assembly of the title structures, called 2-methylbenzylammonium chloride and 3-methylbenzylammonium chloride, since the amine cations interact with the chloride anions through weak hydrogen bonds type N-H…Cl and C-H…Cl and C-H…π interactions, so that both compounds belong to Class I of hybrids. These compounds were studied by X-ray diffraction to determine the crystallographic characteristics and atomic arrangements, Hirshfeld analysis, and infrared spectroscopy are discussed. Moreover, theoretical calculations were undertaken with the aim to elucidate the correlation

between the molecular structure, optical property, and charge transfer interactions. Thermal studies (DTA-TG) have also been undertaken and reported.

2. Experimental section

2.1. Materials

All reagents: The cadmate chloride monohydrate (purity 98%), Hydrochloric acid (HCl; 37%), 2-methylbenzylamine (purity 96%), and 3-methylbenzylamine (purity 98%) were used as received from Sigma-Aldrich, without further purification.

2.1.1. Synthesis of (2-$CH_3C_6H_4CH_2NH_3$)Cl (1)

A solution of 2-methylbenzylamine (2 mmol, 242 mg) was dissolved in ethanol, and $CdCl_2.H_2O$ (1 mmol, 201 mg) mixed in dilute HCl (10 mL, 3M) was added. The mixture is left under stirring at room temperature for 1 h. One week later fine colorless needles single crystals were formed (240 mg). The yield of the reaction is about 76 %. Anal. Calc.: C, 60.97%; H, 7.62%; N, 8.89%. Found: C, 60.80%; H, 7.58%; N, 8.83%. Melting point temperature = 489 K.

2.1.2 Synthesis of (3-$CH_3C_6H_4CH_2NH_3$)Cl (2)

An aqueous solution containing (1 mmol, 201 mg) of $CdCl_2.H_2O$ mixed in dilute HCl (10 mL, 3M) was added drop wise to 3-methylbenzylamine (1 mmol, 141 mg) in 10 mL of ethanol. The obtained solution was stirred for several minutes and then filtered using Whatman filter paper.

The colorless crystals appeared after few days (129 mg, yield 82 %). Elemental analysis, Calc.: C, 60.97%; H, 7.62%; N, 8.89%. Found: C, 61.01 %; H, 7.83 %; N, 8.79 %. Melting point temperature = 482 K.

2.2. X-ray data collection and physical measurements

X-ray diffraction data were collected at 150 K using an APEXII Bruker-AXS diffractometer equipped with Graphite monochromator and MoKα radiation (λ = 0.71073 Å). Absorption corrections were performed by the multi-scan technique using the SADABS program **[24].** The two structures were solved by direct methods with SHELXT **[25],** which revealed the position of all non-hydrogen atoms, and then refined by the full-matrix least-squares methods on $F^2$with SHELXL **[26]** included in the WINGX program **[27].** A summary of the crystal

data and the structure refinement parameters are given in **Table 1**. Structure graphics are drawn with DIAMOND program **[28]**. The ORTEP **[27]** view of the asymmetric unit is shown in **Fig. 1** and **Fig. 3**.

IR spectra were recorded at room temperature in the scan range 400-4000 cm^{-1} with a Perkin-Elmer FT-IR 1000 spectrometer using the technique of pellets with KBr as a dispersant. Thermal analysis was performed using a multimodule 92 Setaram analyzer.

2.3. Computational section

The molecular geometry optimization has been performed with the Gaussian 09 software package **[29]** and the GaussView molecular visualization program **[30].** All the quantum-chemical calculations have been performed via the hybrid B3LYP functional and the standard 6-311++G(d,p) basis set **[31,32].** Input geometric structures of these salts are based on the obtained X-ray structure (CIF format). The calculations have converged to optimized geometries that correspond to the lowest energy. Vibrational calculations were performed at the same level of theory to ensure that there are no imaginary frequencies while the positive frequencies obtained confirm the stability of the optimized geometries. The vibrational assignments were carried out using the VEDA4 program **[33].** 3D Hirshfeld surfaces and 2D fingerprint were plotted using Crystal Explorer version 3.1 software **[34]**. To study the excited states, time-depending density functional theory (TD-DFT) **[35]** calculations were performed on the optimized structures at the same level of theory.

3. Results and discussion

3.1. X-ray diffraction and molecular modeling

3.1.1. Structure description of (1)

The asymmetric unit of (1) depicted in an ORTEP drawing (**Fig.1a**), is formed by a monoprotonated 2-methylbenzylammonium cation and one chloride anion Cl^-.

The packing of the structure, viewed along the *bc* plane (**Fig. 2a**), shows a double layer of 2-methylbenzylammonium cations in zigzag distribution along b-axis in z = 0 and z = ½, embedded between two consecutive chloride anions. The organic cations and the chloride anions are linked via N–H…Cl hydrogen bonds, with donor-acceptor distances ranging from 3.151 (2) to 3.222 (2)Å (details in **Table 3**), and where all hydrogen atoms attached to N are involved. Because of the steric hindrance of the organic component, the distance between the

mean planes of two adjacent chloride anions is remarkably high. The chloride anions form pillars running along the b-axis direction (**Fig. 2a**). These pillars are located around z = ¼, and ¾. Two prominent hydrogen bonding motifs can be mentioned with the supposed graph set descriptors **[36]:** Inside a pillar the N–H…Cl hydrogen bonds between ammonium groups and chloride anions in the crystal network form 8-membered rings (graph set descriptor: $R_4^2(8)$, (**Fig. 2b**). Further, a simple chain motif is seen, which is formed by the chloride anions and the ammonium groups (graph set descriptor: $C_2^1(4)$, (**Fig. 2a).** Consequently, a chain-type polymer is formed, which propagates along the crystallographic b axis. Organic cations are also close enough to enable a C–H…π interaction to occur with a distance of 3.6358 Å and connect in a chain along a-axis (**Fig. 2b**). These two last interactions ensure the stabilization of the crystal structure in the solid-state.

The optimized molecular structure of compound (1) is given in (**Fig.1b**) in order to investigate the effects of intermolecular interactions on geometrical parameters. A comparison between selected experimental X-ray crystallographic parameters, with the optimized parameters, is given in **Table 2**.

Assessment of the organic geometrical features (**Table 2**) shows that the 2-methylbenzylammonium cation exhibits a normal spatial configuration quite similar to the usual values observed in others homologous derivates **[18, 19, 37].** The calculated values of binding lengths of the aromatic ring are almost identical to those observed experimentally by X-ray diffraction, the (C−C) bond lengths varying from 1.378(3) to 1.394(3) Å were calculated at the range 1.39-1.4 Å and (C−C−C) bond angles around 120° confirming the good flatness of the cycle. The aromatic ring has a plane geometry disubstituted in C2 and C7 position, a methyl (−CH_3) coplanar with the phenyl group on the C2 atom and a group (−CH_2−NH_3) on the C7 atom. The linkage length of the methyl group bound to N is, C8-N9 = 1.490 Å and the N9—C8—C7 bond angle is 112.35° (18), which are close to the calculated values (1.503 Å, 111.434°).

3.1.2. Structure description of (2)

The asymmetric unit of (2), consists of a monoprotonated 3-methylbenzylammonium molecule and one chloride anion Cl^- (**Fig.3**).

The bidimensional arrangement is shown in **Fig. 4a**, in which a double layer of 3-methylbenzylammonium cations in zigzag distribution along b-axis in z = 1/4 and z = 3/4, is embedded between two consecutive chloride anions that form pillars around z = 0, and ½

along the b-axis. The same stacking interactions were also observed for the 2-methylbenzylammonium chloride. The organic cations and the chloride anions are linked via N–H…Cl and C-H…Cl hydrogen bonds, with donor-acceptor distances ranging from 3.119 (11) to 3.175 (14) Å and from 3.756 (18) to 3.757 (18), respectively (details in **Table 3**). **Fig. 4c&d** depicts that each organic cation participates in the structure cohesion through N–H···Cl hydrogen bonds form hexagonal double rings with $R_6^3(12)$ motifs, other generated rings form $R_4^2(8)$ motifs (**Fig. 4d**). Organic cations are also connected together via C–H…π interactions (**Table 3**) (**Fig. 4b**) to provide the cohesion and the stability of the two dimensional supramolecular architecture.

DFT calculations were also applied on compound (2) (**Fig. 3b**) at B3LYP/6-311++ G(d,p) level, experimental, and theoretical geometric parameters are tabulated in **Table 2**.

The bond lengths and angles within the 3-methylbenzylammonium are close to the usual values observed in others compounds with the same organic cation **[17]** (**Table 2**), with(C−C) bond lengths of 1.39 Å and calculated to be relatively equal to the experimental value, the (C−C−C) bond angles are of 120°. The aromatic ring is disubstituted in C2 and C6 position, a methyl (−CH_3) coplanar with the phenyl group on the C2 atom and a group (−CH_2−NH_3) on the C6 atom. The linkage length of the methyl group bound to N is, C8-N9 = 1.492 (17) Å and the N9—C8—C6 bond angle is 112.9° (11), which are close to the calculated values (1.485 Å, 114.129°).

A comparison between 2-methylbenzylammonium chloride and 3-methylbenzylammonium chloride shows that they differ by the position of CH_3 and CH_2-NH_3 on the phenyl ring and by C-H…Cl hydrogen bonds type that exists only in compound (2). However, strong similarities in both structures are observed. These two compounds adopt a layered hybrid-motif and crystallize in the noncentrosymmetric space group $P2_12_12_1$. Likewise as in (1), the asymmetric unit of (2) consists of the organic cation and the chloride anion.

3.2. Hirshfeld surface analysis

Hirshfeld surfaces have been applied as a use full approach to provide an additional insight on the influence of weak interactions as well, as quantify their individual contribution in the crystal packing. The Hirshfeld d_{norm} surfaces of compounds 1and 2 along with the shape index and the curvedness cartography are shown in **Fig. 5**. The 2D fingerprint plots of the

intermolecular contacts for both compounds (1) and (2) are shown in **Figs. 6** and **7** and the calculated values of the enrichment ratios in the two compounds are given in **Table 4.**

In compound (2-$CH_3C_6H_4CH_2NH_3$)Cl(1), intensive red spots are observed on the d_{norm} surface which corresponds to N–H…Cl hydrogen bonds (**Fig. 5a**), while red and blue triangles observed on the Shape index cartography (**Fig. 5b**) and large flat regions delimited by a blue outline around the aromatic nuclei observed on the Curvedness graph corresponds to C-H... π interactions (**Fig. 5c**).

Examining 2D graphs (**Fig. 6**) highlights atoms involved in close contact. In fact, the major contribution (52.9%) comes from H…H intercontacts that appear as a single broad peak in the middle of the scattered points, which point towards the origin and correspond to (d_e + d_i ~ 2.1 Å), a values lightly less than the sum of the VdW radii of the atoms of hydrogen (2.18 Å). H ... H contacts appear with an enrichment ratio close to unity (0.91), this value agrees well with Jelch's expectation **[38]**. The second major contribution (27.8%) comes from H…Cl/Cl…H intercontacts corresponding to the N−H…Cl interactions, appear as two-pointed symmetrical spikes with a maximum sum of d_e + d_i ~ 2.2 Å less than the sum of the VdW radii of the chlorine atom and the hydrogen atom (1.75 + 1.09 = 2.84 Å) and are moderately enriched with an enrichment ratio ER = 1.31.

These findings affirm that the last two intercontact are considered to be close contacts.

The contacts H…C/C…H cover 18.1% of the overall surface of Hirshfeld show on its 2D graph the presence of symmetric pair of wings around a sum (d_e+ d_i ~ 2.8 Å) greater than the sum of the VdW radii of the carbon and hydrogen atoms (2.79 Å) which exclude these contacts from being close. On the other hand, the contacts H…C/C…Hare slightly favored in a sample of aromatic molecules with an average value of ER_{CH} = 1.17, this important value (> 0.8) indicates the presence of C-H... π interactions **[8].**

The C…C contacts, which represent only 0.2% of the Hirshfeld surface with (d_e + d_i ~3.7 Å) greater than the sum of the VdW radii of the carbon atoms (3.4 Å), reveals the absence of close C…C contacts.

In compound (3-$CH_3C_6H_4CH_2NH_3$)Cl (2), intensive red spots are observed on the d_{norm} surface which correspond to N–H…Cl and C-H…Cl hydrogen bonds (**Fig. 5d**).

Examining 2D graphs shown in **Fig. 7** highlights atoms involved in close contact. H…H intercontacts have the most significant percentage contributions to the surface of

Hirshfeld 51% and appear in the middle of the scattered points by two weak peaks around (d_e + d_i ~ 2.3 Å), a value greater than the sum of the VdW radii of the atoms of hydrogen, reveals the absence of close H…H contacts. These contacts occupy more than three quarter of HS with S_H= 75.4% and an enrichment ratio of 0.89. The second major contribution (31.7%) comes from H…Cl/Cl…H intercontacts, with a sum of d_e + d_i ~ 2.2 Å less than the sum of the VdW radii of the chlorine atom and the hydrogen atom. The value (ER_{HCl} = 1.32) greater than unity, of H…Cl/Cl…H contacts show the propensity to form N-H ... Cl, and C-H ... Cl hydrogen bonds. The H…C/C…H contacts comprise 17.1% of the entire surface of Hirshfeld around a sum (d_e+ d_i ~ 2.8 Å) greater than the sum of the VdW radii of the carbon and hydrogen atoms (2.79 Å). On the other hand, H…C/C…H contacts have an enrichment ratio equal to 1.29, which also proves the presence of C-H... π interactions. This is also confirmed by the presence of the red and blue triangles on the Shape index cartography (**Fig. 5e**) and in the large flat regions delimited by a blue outline around the aromatic nuclei observed on the Curvedness graph (**Fig. 5f**).

Fig. 7d shows the pairs (d_i, d_e) of carbon atoms. It can be seen that (d_e + d_i ~ 3.6 Å)> 3.4 Å, the sum of the VdW radii of the carbon atoms.

Such visual analysis of intermolecular interactions is consistent with those found by X-ray diffraction analysis for both compounds.

3.3. Vibrational analysis

Herein, the vibrational behavior in the solid-state of both compounds is discussed. The theoretical and experimental spectra are shown in **Fig. 8** for (1) and **Fig. 9** for (2).The experimental infrared wavenumber and the calculated one from the DFT method assigned by VEDA program **[33]** and GaussView software **[30]** are provided in **Table 5** and **Table 6,** the correlation between these last two is reasonable. For vibrational frequency, uniform scaling factors proposed by Rauhut and Pulay **[39]** were adopted: frequencies below 1700 were multiplied by 0.983, and greater than 1700 were multiplied by 0.958 **[40-44].** This correction is made to find a good agreement with the experimental frequencies, the slight differences observed are attributed to the calculations since they were performed in the gas phase. The detailed assignment of the characteristic bands is essentially based on comparisons with data previously reported for similar materials. PED calculations were carried out with the aid of the VEDA program **[33]**, as well as the automatic optimization of PED contributions which is a unique feature of the VEDA program **[45]**.

- **Ring vibration of (1) and (2)**

The band exhibited between 3054-2878 cm^{-1} for (1) and between 3018-2920 cm^{-1} for (2) is due to the aromatic C-H stretching vibration and predicted between 3057-2891cm^{-1} and between 3048-2898cm^{-1} respectively.

The single strain band in the theoretical spectrum located at 765 cm^{-1} in **Fig.8** and at 1473 cm^{-1} in **Fig. 9** correspond to the C-H out-of-plane bending vibration and shows the existence of a –1,2 disubstitution in compound (1) and a –1,3 disubstitution in compound (2); especially since it is an intense tape.

The bands between 1634-1571 cm^{-1} for (1) and between 1594-1473 cm^{-1} for (2) are attributed to the C=C stretching vibration of the aromatic ring and predicted between 1616-1588 and 1618-1598 cm^{-1}. The spectral domain between 761 and 454 cm^{-1} for (1) and between 784 and 440 cm^{-1} for (2) is ascribed to the out of plane vibration modes of the δ(C-C) and δ(C=C) groups. This was calculated to be found in regions 765-413cm^{-1} and 788-408 cm^{-1}.

- **Vibration modes of R-NH_3^+ groups in (1) and (2)**

Both of the organic cations belongs to the class of primary amines. The two valence asymmetric and symmetric vibrations ν(−N-H) are manifested by strong broad band in the high-frequency region between 3435-3423 cm^{-1} for (1) and between 3435-3429 cm^{-1} for (2). The DFT computations give the frequency of these bands between 3393 and 3319 cm^{-1} for (1) and 3404-3332 cm^{-1} for (2).

The characteristic NH_3^+ asymmetric and symmetric stretching vibrations are in the same region with the C=C stretching vibration and the frequencies are in good agreement with those predicted theoretically.

The bands that lie between 952 and 907 cm^{-1} for (1) and between 969-903 cm^{-1} for (2) in the experimental spectrum correspond to the C-N and C-C stretching. The same vibration is calculated between 954-939 cm^{-1} and 1029-874 cm^{-1} by DFT level. In 3-methylbenzylammonium trioxonitrate **[17]** these modes are observed nearly in the same region.

The calculated wavenumbers of the two salts were in good agreement with the experimental data.

3.4. Frontier orbitals and chemical quantum descriptors

The 3D plots of the four important FMOs (HOMO, HOMO−1, LUMO and LUMO+1) of both compounds (1) and (2) are provided in **Fig.10** and **Fig.11,** respectively. The global chemical reactivity descriptors were as well defined; the results of this survey using the TD-DFT approach are gathered in **Table 7** for compound (1) and **Table 8** for compound (2).

Orbital analysis in both cases of salts revealed that the HOMO components are located on the chloride anion and the organic part, while the LUMO components are mainly located on the NH_3^+ group and the benzene ring. The positive and the negative phase are represented by the red and the green colors, respectively. For compound (1), the space of energy between HOMO-LUMO molecular orbitals calculates 5.00 eV, which is an index of high kinetic stability and low chemical reactivity. Besides gap energy, hardness (η =2.5) and chemical softness (S =0.19) indicate that the flow of electrons in the higher energy states is difficult, which makes the molecule hard **[49,47]**. For compound (2), the energy gap value is equal to 5.03 eV. This value agrees very well with the corresponding energy gap reported earlier with the same organic cation **[17]**.

Moreover, the electrophilicity index ($\omega = \mu^2/2\eta$ **[48]**) is about 9.9775 eV for compound (1) and 9.8083 eV for compound (2), according to these values, we can conclude that compound (1) is a good electrophile somewhat better than compound (2). Therefore, it is capable of accepting an electron doublet in order to form bonds with another reagent which is necessarily a nucleophile. Electronegativity is also determined (χ = (I+A)/2 **[49]**) and it is found to be χ =7.0639 eV and χ =7.0296 eV for compound (1) and (2), respectively.

3.5. Molecular electrostatic potential (MEP)

The molecular electrostatic potential surface (MEPs) map of both compounds calculated at the B3LYP/6-311++G(d,p) level of theory is shown in **Fig. S1.** MEPs is a graph of the electrostatic potential mapped on a surface with a constant electron density, its value lies in visualizing the charge distributions, the exploration of hydrogen bonding interactions, and in depicting the molecular shape and size. For these reasons, it was employed in numerous studies **[50-52].**

The electronic distribution can be easily seen from the different colorations of their mapped surfaces; the latter is color-coded and subdivided into many regions where these

different colors are used to identify the different potentials. Blue and red colors indicate positive and negative potentials, respectively.

The area of negative potentials (excess in electrons) appear to be distributed on the Chloride anions as a nucleophilic site while the most positive potential (deficient in electrons) is observed near the $-NH_3^+$ group of the 2-methylbenzylammonium and the 3-methylbenzylammonium cations so candidates for nucleophilic attacks. On the cation side chain in both compounds a notable pale yellow color typical of a slightly inert region is observed. This confirms the existence of intermolecular N-H···Cl interactions between the organic cations and the Cl^- anions.

The charge distribution is not the same in both cases of salts and was influenced by the chemical environment. This difference can be attributed to the spatial arrangement of every halogen in the structure of each salt.

3.6. Non-linear optical properties

The electric dipole moment, polarizability, and first-order hyperpolarizability values of the title materials using DFT/B3LYP method are grouped in **Table S1** and **Table S2.** These quantities are obtained from the following equations:

$$\mu_{tot} = (\mu_x^2 + \mu_y^2 + \mu_z^2)^{1/2}$$

$$\alpha_{tot} = \frac{1}{3}(\alpha_{xx} + \alpha_{yy} + \alpha_{zz})$$

$$\beta_{tot} = [(\beta_{xxx} + \beta_{xyy} + \beta_{xzz})^2 + (\beta_{yyy} + \beta_{yzz} + \beta_{yxx})^2 + (\beta_{zzz} + \beta_{zxx} + \beta_{zyy})^2]^{1/2}$$

The values of α and β from the Gaussian output are in atomic units (a.u.), the conversion into the electronic units (esu) is:(α; 1 a.u. = 0.1482×10^{-24} esu, β; 1 a.u. = 8.6393×10^{-33} esu).

The calculated values of the dipole moment, the polarizability, and the first-order hyperpolarizability of compound (1) are respectively 7.5990 Debye, 10.8×10^{-24} esu, and 899.69×10^{-33} esu and for the second compound (μ= 6.6165 Debye, $\alpha= 11.4\times10^{-24}$ esu, β= 1525.98×10^{-33} esu). The comparison of these results with the urea which is a standard NLO reference material (μ= 1.3732 Debye, $\alpha= 5.0477\times10^{-24}$ esu, β= 372.8×10^{-33} esu) **[53],** shows a large value of β_{tot} in both cases, indicating an important second-order optical effect. For compound (1)β_{tot} is higher than 2x β_{urea} and for compound (2) β_{tot} is a bit higher than 4x β_{urea}. This latter is more important because unlike the compound (1) two types of H-bonds (N-H…Cl and C-H…Cl) exists in its crystal structure and by reference to the literature **[54, 55]**,

hydrogen bonds contribute to the improvement of the hyperpolarizability of molecular systems and therefore the enhancement of the optical properties of the materials.

Moreover, in both cases of salts, the calculated polarizability α_{tot} is found to be higher than $2\alpha_{urea}$ and the dipole moment is 5 times higher than μ_{urea}, which can be explained by the non-centrosymmetric nature of these molecules. For compound (1) the highest absolute value of the dipole moment is observed for the component μ_x in this direction the value is equal to 5.64 D. All these findings nominate both salts as good materials for NLO application.

3.7. Thermal behavior

The thermal stability of both compounds was studied simultaneously by DTA (Differential Thermal Analysis) and by TG (Thermogravimetric Analysis) in rising of the ambient temperature up to 673 K with a constant heating rate of 5° C min^{-1} and under argon flow. The total amount of product used for the analysis of compound (1) and (2) was 10.8 mg and 11.5 mg, respectively.

The observed thermal behavior is illustrated in **Fig.S2**. The DTA curve shows that the sharp endothermic peak without loss of mass located at 489 K in **Fig. S2a** and at 482K in **Fig. S2b** is attributed to the melting of the compounds. This value is further confirmed by heating the compounds on a Kofler bench (473 K for compound (1) and 459K for compound (2)), this value is comparable with other compounds with the same organic cations **[17].** In the last stage, the strong endothermic mass loss process occurs in a single step. This step (see **Fig. S2a** &**b)** corresponds to the pyrolysis of the organic part.

Conclusion

Thus, two new organic salts have been synthesized while attempting to synthesize organic-chlorocadmate assembly. The newly synthesized salts were grown at room temperature by the slow solvent evaporation technique; both compounds 1 and 2 adopt a layered hybrid-motif and crystallize in the noncentrosymmetric space group $P2_12_12_1$. Single crystal X-ray structure determination revealed that the crystal packing consists of Cl^- anions and $(C_8H_{12}N)^+$cations interconnected via hydrogen bonds, electrostatic, and van der Waals interactions creating a two-dimensional network. The Hirshfeld surface analysis of the crystal structure shows that the H…H and H…Cl/Cl…H contacts constitute the main driving force in the crystal packing formation. The vibrational wavenumbers of the fundamental modes have

been precisely analyzed, assigned, by comparison with the vibration modes frequencies of homologous compounds, and the theoretical results were compared with the experimental values. The TG/DTA thermal analysis was performed to study the thermal behavior. Both compounds are found to be good candidates for nonlinear optical applications.

Acknowledgements

We are grateful to the Tunisian Ministry of Higher Education Scientific Research for the provided support.

References

[1] M. A. Fashapoyeh, M. Mirzaei, H. Eshtiagh-Hosseini, A. Rajagopal, M. Lechner, R. Liu, C. Streb, Photochemical and electrochemical hydrogen evolution reactivity of lanthanide-functionalized polyoxotungstates. Chem. Commun. 54 (2018) 10427-10430.

[2] S. Derakhshanrad, M. Mirzaei, C. Streb, A. Amiri, C. Ritchie, Polyoxometalate-based frameworks as adsorbents for drug of abuse extraction from hair samples, Inorg. Chem. 60 (2021) 1472-1479.

[3] Z. Khoshkhan, M. Mirzaei, H. Eshtiagh-Hosseini, M. Izadyar, J. T. Mague, M. Korabik, Two polyoxometalate-based hybrids constructed from trinuclear lanthanoid clusters with single-molecule magnet behavior. Polyhedron, 194 (2021) 114903.

[4] M. Samaniyan, M. Mirzaei, R. M. Gomila, H. Eshtiagh-Hosseini, N. Lotfian, J. T. Mague, J. T., A. N. Pour, A. Frontera, Supramolecular network of a framework material supported by the anion–π linkage of Keggin-type heteropolyoxotungstates: experimental and theoretical insights, Dalton Trans. 50 (2021) 1895-1900.

[5] M. Akbari, M. Mirzaei, A. Amiri, Synergistic effect of lacunary polyoxotungstates and carbon nanotubes for extraction of organophosphorus pesticides. Microchemical Journal, 170 (2021) 106665.

[6] M. Arefian, M. Mirzaei, H. Eshtiagh-Hosseini, A. Frontera, A survey of the different roles of polyoxometalates in their interaction with amino acids, peptides and proteins. Dalton Trans. 46 (2017) 6812-6829.

[7] A. Najafi, M. Mirzaei, J. T. Mague, Structural scope of six new layered to pillar-layered hybrid inorganic–organic networks bearing $[BW_{12}O_{40}]^{5-}$ and lanthanoid-cluster; database study toward ligand role in assemblies. CrystEngComm, 18 (2016) 6724-6737.

[8] I. Jomaa, O. Noureddine, S. Gatfaoui, N. Issaoui, T. Roisnel, H. Marouani, Experimental, computational, and in silico analysis of $(C_8H_{14}N_2)_2[CdCl_6]$ compound, J. Mol. Struct. 1213 (2020) 128186.

[9] C. Ben Mleh, T. Roisnel, H. Marouani, Crystal Structure, Infrared spectroscopy and Hirshfeld Surface Analysis of a New Organic–Inorganic Hybrid Compound: Quinolinium Dihydrogenphosphate. J. Chem. Crystallogr., 46 (2016) 345–351.

[10] I. Jomaa, N. Issaoui, T. Roisnel, H. Marouani, Insight into non-covalent interactions in a tetrachlorocadmate salt with promising NLO properties: Experimental and computational analysis, J. Mol. Struct., 1242 (2021) 130730.

[11] M. Vimalan, A. Ramanand, P. Sagayaraj, Synthesis, growth and characterization of l-alaninium oxalate – a novel organic NLO crystal, Cryst. Res. Technol., 42 (2007) 1091-1096.

[12] C. Ben Mleh, S. A. Brandán, N. Issaoui, T. Roisnel, H. Marouani, Synthesis, molecular structure, vibrational and theoretical studies of a new non-centrosymmetric organic sulphate with promising NLO properties. J. Mol. Struct., 1171 (2018) 771-785.

[13] M. Essid, S. Muhammad, H. Marouani, A. Saeed, Z. Aloui, A. G. Al-Sehemia, Synthesis, characterization, Hirshfeld surface analysis and computational studies of 1-methylpiperazine-1,4-diium bis(hydrogen oxalate): $[C_5H_{14}N_2](HC_2O_4)_2$, J. Mol. Struct., 1211 (2020) 128075.

[14] F. Markwardt, H. Landmann, P. Walsmann, Comparative Studies on the Inhibition of Trypsin, Plasmin, and Thrombin by Derivatives of Benzylamine and Benzamidine, Eur. J. Biochem. 6 (1968) 502–506.

[15] K. Lee, W. H. Jung, C. W. Park, C. Y. Hong, I. C. Kim, S. Kim, Y. S. Oh, O H. Kwon, S.H. Lee, H. D. Park, S.W. Kim , Y.H. Lee, Y. J. Yoo, Benzylamine-based selective and orally bioavailable inhibitors of thrombin. Bioorg. Med. Chem. Lett., 8 (1998) 2563-2568.

[16] A. Obreza, M. Stegnar, U. Urleb, Novel non-covalent azaphenylalanine thrombin inhibitors with an aminomethyl or amino group at the P1 position, Pharmazie, 59 (2004) 659-667.

[17] S. Gatfaoui, N. Issaoui, T. Roisnel, H. Marouani, Synthesis, experimental and computational study of a non-centrosymmetric material 3-methylbenzylammonium trioxonitrate, J. Mol. Struct., 1225 (2021) 129132.

[18] R. Aarthi, A. A. Thiruvalluvar, C. Ramachandra Raja, Bis(4-methyl-benzyl-ammonium) tetra-bromido-zincate, IUCrData, 3 (2018) 180648.

[19] R. Aarthi, P. Umarani, C. Ramachandra Raja, Molecular structural confirmation and influence of hydrogen bond on third order nonlinear properties of bis(4-methylbenzylammonium) tetrachloridocadmate(II) single crystal, Optik 164 (2018) 449–454.

[20] U.J. Luelf, G.J. Reiss, A Bokel, V. B. Urlacher, Selective biocatalytic synthesis and crystal structure of (2R,6R)-hydroxyketaminium chloride, $C_{13}H_{17}Cl_2NO_2$, Z. Kristallogr. New Cryst. Struct., 236 (2021) 827-829.

[21] N. Brandt, G.J. Reiss, The twinned crystal structure of 1,3-phenylenedimethanaminium dibromide, $C_8H_{14}Br_2N_2$, Z. Kristallogr. New Cryst. Struct., 236 (2021) 519-521.

[22] H. Cheng, H. Li, (m-Phenylenedimethylene)diammonium dichloride, Acta Crystallogr. Sect. E Struct. Rep. Online 64 (2008) o2060.

[23] I. Hamdi, I. Bkhairia, A. Roodt, T. Roisnel, M. Nasri, H. Naïli, Synthesis, intermolecular interactions and biological activities of two new organic–inorganic hybrids $C_6H_{10}N_2$,2Br and $C_6H_{10}N_2$,2Cl·H_2O. RSC Adv. 10 (2020), 5864-5873.

[24] Bruker, APEX2, SAINT and SADABS, Bruker AXS Inc., Madison, Wisconsin, USA, 2006.

[25] G. M. Sheldrick, SHELXT–Integrated space-group and crystal-structure determination, Acta Crystallogr. A, 71 (2015) 3-8.

[26] G.M. Sheldrick, Crystal structure refinement with SHELXL, Acta Crystallogr., Sect. A: Found. Crystallogr. A, 64 (2008) 112-122.

[27] L. J. Farrugia, WinGX and ORTEP for windows: an update, J. Appl. Cryst. 45 (2012) 849-854.

[28] G. Bergerhoff, M. Berndt, K. Brandenburg, Evaluation of Crystallographic Data with the Program DIAMOND, J. Res. Natl. Inst. Stand. Technol., 101 (1996) 221–225.

[29] M.J. Frisch, G.W. Trucks, H.B. Schlegel, G.E. Scuseria, M.A. Robb, J.R. Cheeseman, G. Scalmani, V. Barone, B. Mennucci, G.A. Petersson, H. Nakatsuji, M. Caricato, X. Li, H.P. Hratchian, A.F. Izmaylov, J. Bloino, G. Zheng, J.L. Sonnenberg, M. Hada, M. Ehara, K. Toyota, R. Fukuda, J. Hasegawa, M. Ishida, T. Nakajima, Y. Honda, O. Kitao, H. Nakai, T. Vreven, J.A. Montgomery Jr., J.E. Peralta, F. Ogliaro, M. Bearpark, J.J. Heyd, E. Brothers, K.N. Kudin, V.N. Staroverov, R. Kobayashi, J. Normand, K. Raghavachari, A. Rendell, J.C. Burant, S.S. Iyengar, J. Tomasi, M. Cossi, N. Rega, J.M. Millam, M. Klene, J.E. Knox, J.B. Cross, V. Bakken, C. Adamo, J. Jaramillo, R. Gomperts, R.E. Stratmann, O. Yazyev, A.J. Austin, R. Cammi, C. Pomelli, J.W. Ochterski, R.L. Martin, K. Morokuma, V.G. Zakrzewski, G.A. Voth, P. Salvador, J.J. Dannenberg, S. Dapprich, A.D. Daniels, O. Farkas, J.B. Foresman, J.V. Ortiz, J. Cioslowski, D.J. Fox, Gaussian, Inc., Wallingford CT, 2009.

[30] R. Dennington, T. Keith, J. Millam, GaussView, Version 5, Semichem. Inc Shawnee Mission, KS, 2009.

[31] A.D. Becke, Becke's three parameter hybrid method using the LYP correlation functional, J. Chem. Phys. 98 (1993) 5648-5652.

[32] C. Lee, W. Yang, R.G. Parr, Development of the Colle-Salvetti correlation-energy formula into a functional of the electrondensity, Phys. Rev. B37 (1988) 785.

[33] M.H. Jamróz, Vibrational Energy Distribution Analysis: VEDA 4, 2004.

[34] S.K. Wolff, D.J. Grimwood, J.J. McKinnon, D. Jayatilaka, M.A. Spackamn, CrystalExplorer 3.1, University of WestrenAustralia, Perth, 2013.

[35] M. E. Casida, C. Jamorski, K. C. Casida, D. R. Salahub, Molecular excitation energies to high-lying bound states from time-dependent density-functional response theory: Characterization and correction of the time-dependent local density approximation ionization threshold, J. Chem. Phys. 108 (1998) 4439-4449.

[36] J. Grell, J. Bernstein, G. Tinhofer, Investigation of hydrogen bond patterns: a review of mathematical tools for the graph set approach. Crystallogr. Rev. 8 (2002) 1–56.

[37] Y. Jin, C.H. Yu, W. Zhang, Structural diversity of a series of chlorocadmate(II) and chlorocuprate(II) complexes based on benzylamine and its N-methylated- derivatives, J. Coord. Chem. 67 (2014) 1156.

[38] C. Jelsch, K. Ejsmont, L. Huder, The enrichment ratio of atomic contacts in crystals, an indicator derived from the Hirshfeld surface analysis, L. IUCrJ, 1 (2014) 119–128.

[39] G. Rauhut, P. Pulay, Transferable Scaling Factors for Density Functional Derived Vibrational Force Fields, J. Phys. Chem., 99 (1995) 3093-3100.

[40] C. Daghar, N. Issaoui, T. Roisnel, V. Dorcet, H. Marouani, Empirical and computational studies on newly synthesis cyclohexylammonium perchlorate, J. Mol. Struct. 1230 (2021) 129820.

[41] A. Sagaama, N. Issaoui, Design, molecular docking analysis of an anti-inflammatory drug, computational analysis and intermolecular interactions energy studies of 1-benzothiophene-2-carboxylic acid, Comput. Biol. Chem. 88 (2020) 107348.

[42] M. Tahenti, S. Gatfaoui, N. Issaoui, T. Roisnel, H. Marouani, A tetrachlorocobaltate(II) salt with 2-amino-5-picolinium: synthesis, theoretical and experimental characterization, J. Mol. Struct. 1207 (2020) 127781.

[43] I. Hamdi, N. Mhadhbi, N. Issaoui, A. Roodt, M. M. Turnbull, H. Naïli, Design, synthesis and physico-chemical studies of a Co (II)/Co (III) mixed-valence complex: An experimental and DFT approach, J. Mol. Struct. 1237 (2021) 130384.

[44] J. Kausteklis, V. Aleksa, M.A. Iramain, S.A. Brandán, Cation-anion interactions in 1-buthyl-3-methyl imidazolium nitrate ionic liquid and their effect on their structural and vibrational properties, J. Mol. Struct. 1164 (2018) 563-576.

[45] M.H. Jamróz, Vibrational energy distribution analysis (VEDA): Scopes and limitations, Spectrochim. Acta A Mol. Biomol. Spectrosc., 114 (2013) 220-230.

[46] R.G. Parr, P.K. Chattaraj, Principle of maximum hardness, J. Am. Chem. Soc. 113

(1991) 1854-1855.

[47] R.G. Parr, R.G. Pearson, Absolute hardness: companion parameter to absolute electronegativity, J. Am. Chem. Soc. 105 (1983) 7512-7516.

[48] R. G. Parr, L. von Szentpaly, S. Liu, Electrophilicity index, J. Am. Chem. Soc. 121 (1999) 1922-1924.

[49] R. S. Mulliken, A new electro affinity scale; together with data on valence states and on valence ionization potentials and electron affinities, J. Chem. Phys. 2 (1934) 782-794.

[50] N. Mohan, C. H. Suresh, A molecular electrostatic potential analysis of hydrogen, halogen and dihydrogen bonds, J. Phys. Chem. 118 (2014) 1697–1705.

[51] S. Trabelsi, N. Issaoui, S.A. Brandán, F. Bardak, T. Roisnel, A. Atac, H. Marouani, Synthesis and physic-chemical properties of a novel chromate compound with potential biological applications, bis(2-phenylethylammonium) chromate (VI), J. Mol. Struct. 1185 (2019) 168–182.

[52] P. Politzer, J. S. Murray, The fundamental nature and role of the electrostatic potential in atoms and molecules, Theor. Chem. Acc. 108 (2002) 134–142.

[53] R. Thirumurugan, B. Babu, K. Anitha, J. Chandrasekaran, Investigation on growth, structure and characterization of succinate salt of 8-hydroxyquinoline: an organic NLO crystal, Spectrochim. Acta A Mol. Biomol. Spectrosc. 140 (2015) 44-53

[54] L.M. Yang, Y. Liu, L.M. Man, J.R. Zhou, X.P. Liu, C.L. Ni, Crystal structure, vibrational spectra, optical properties and density functional theoretical approach of $[Bz\text{-}4\text{-}NH_2\,Py]_4[CdCl_4]_2.H_2O$, Vib. Spectrosc. 93 (2017) 23–28.

[55] P. Asokan, S. Kalainathan, Bulk crystal growth, optical, electrical, thermal, and third order NLO properties of 2-[4(diethylamino)benzylidene]malononitrile (DEBM) single crystal, J. Phys. Chem. C 121 (40) (2017) 22384–22395.

Figure captions

Fig. 1. ORTEP representation of compound (1) with atom-labeling scheme. Displacement ellipsoids are drawn at the 50% probability level. Hydrogen bonds are denoted as dashed lines (a) and the optimized molecular structure (b).

Fig. 2. The packing of compound (1) viewed along the *bc* plane **(a)**,while **(b)** represents a view highlighting intermolecular interactions between organic cations C-H…π stacking and the $R_4^2(8)$ motifs.

Fig. 3. ORTEP representation of compound (2) with atom-labeling scheme. Displacement ellipsoids are drawn at the 50% probability level (a) and the optimized molecular structure (b).

Fig. 4. The packing of compound (2) viewed along the *bc* plane **(a)**, **(b)** represents a view highlighting intermolecular interactions between organic cations C-H…π stacking and **(c,d)** the $R_6^3(12)$ and $R_4^2(8)$ motifs.

Fig. 5. Hirshfeld surfaces mapped with d_{norm} (-0,459 -0,938) (a) (dotted lines "red" represent hydrogen bonds), shape index (-1 - 1) (b) and curvedness (-4 - 0.4) (c) for compound (1), while (d,e,f) represents d_{norm} cartography (-0,515 - 1,196), shape index (-1 -1) and curvedness (-4 – 0.4) of compound (2), respectively.

Fig. 6. 2D fingerprint plots of the main intercontacts of compound (1) showing the percentage of various intermolecular contacts contributed to the Hirshfeld surface.

Fig. 7. 2D fingerprint plots of the main intercontacts of compound (2) showing the percentage of various intermolecular contacts contributed to the Hirshfeld surface.

Fig. 8. Theoretical and experimental IR spectrum of compound (1).

Fig. 9. Theoretical and experimental IR spectrum of compound (2).

Fig. 10. Frontier molecular orbital plots of compound (1) computed with TD-DFT (B3LYP)/ 6-311++G(d,p) method.

Fig. 11. Frontier molecular orbitalplots of compound (2) computed with TD-DFT (B3LYP)/ 6-311++ G(d,p) method.

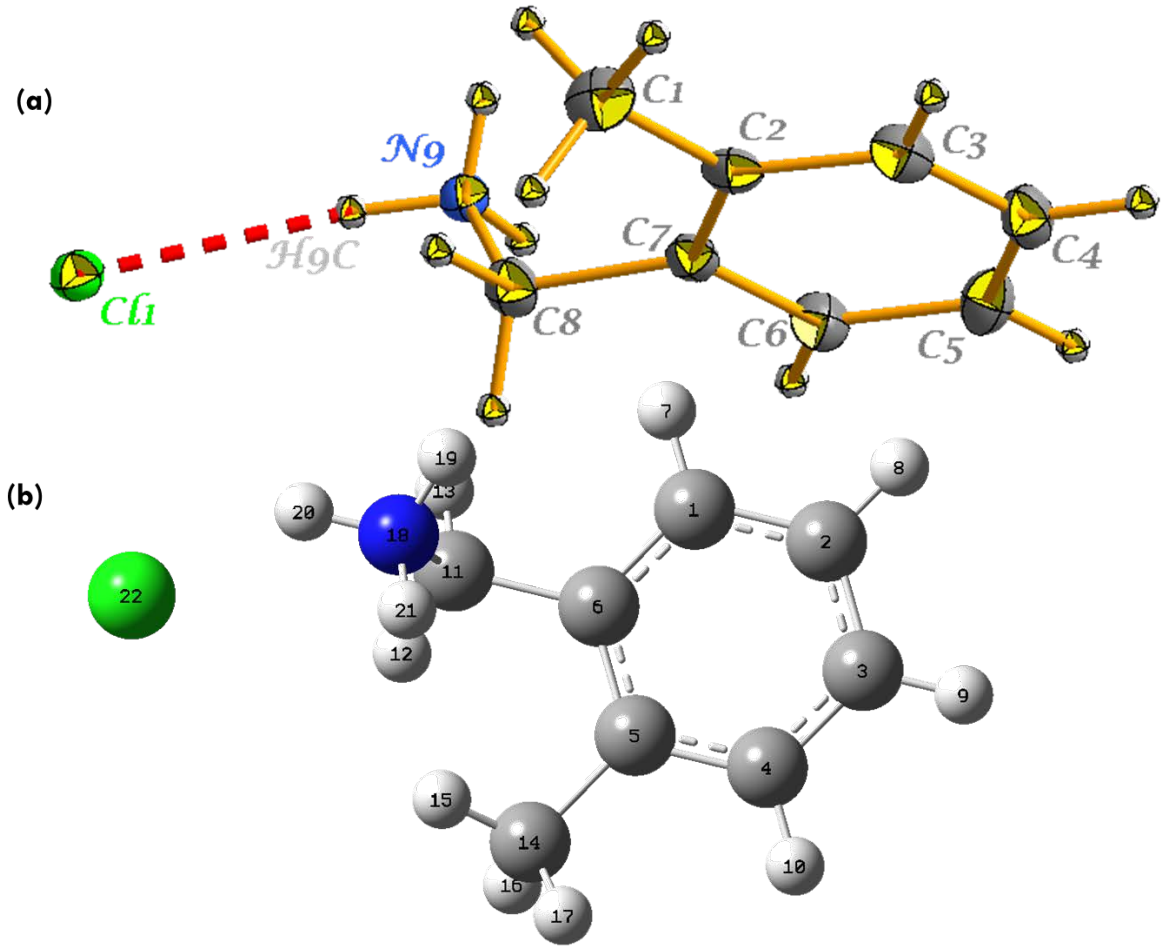

Fig. 1. ORTEP representation of compound (1) with atom-labeling scheme. Displacement ellipsoids are drawn at the 50% probability level. Hydrogen bonds are denoted as dashed lines (a) and the optimized molecular structure (b).

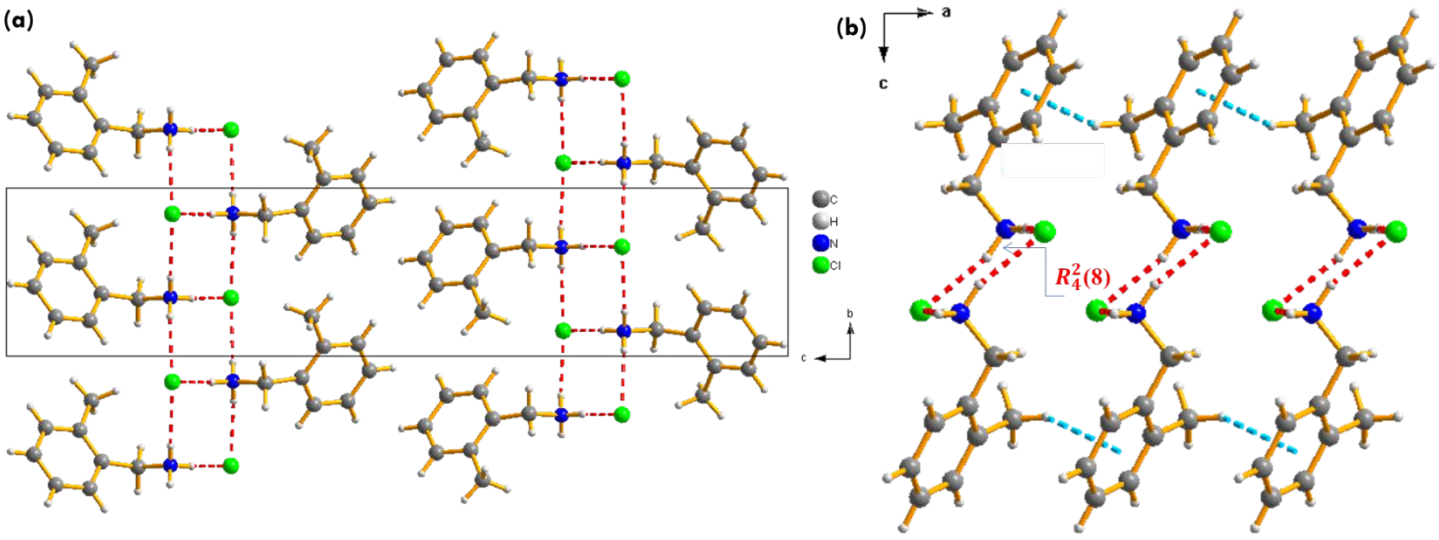

Fig. 2. The packing of compound (1) viewed along the *bc* plane **(a)**, while **(b)** represents a view highlighting intermolecular interactions between organic cations C-H…π stacking and the $R_4^2(8)$ motifs.

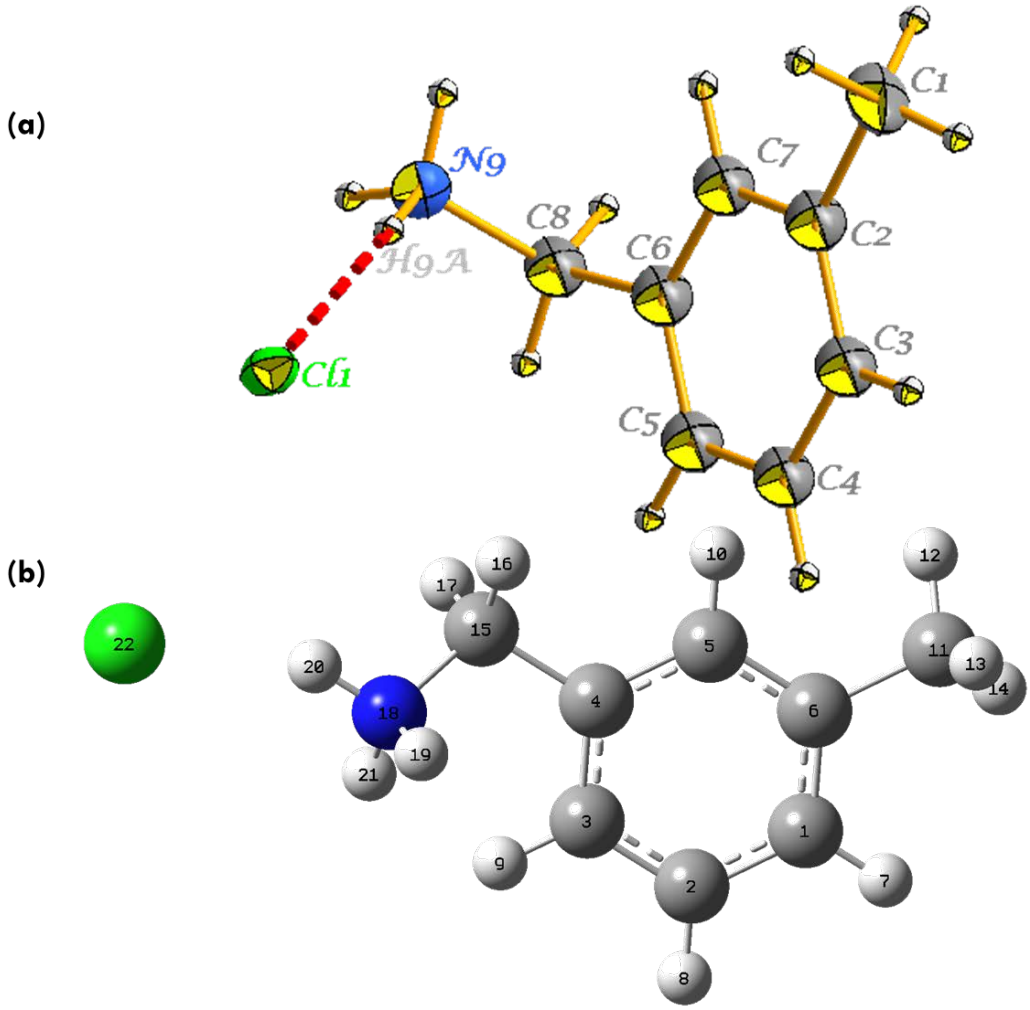

Fig. 3. ORTEP representation of compound (2) with atom-labeling scheme. Displacement ellipsoids are drawn at the 50% probability level (a) and the optimized molecular structure (b).

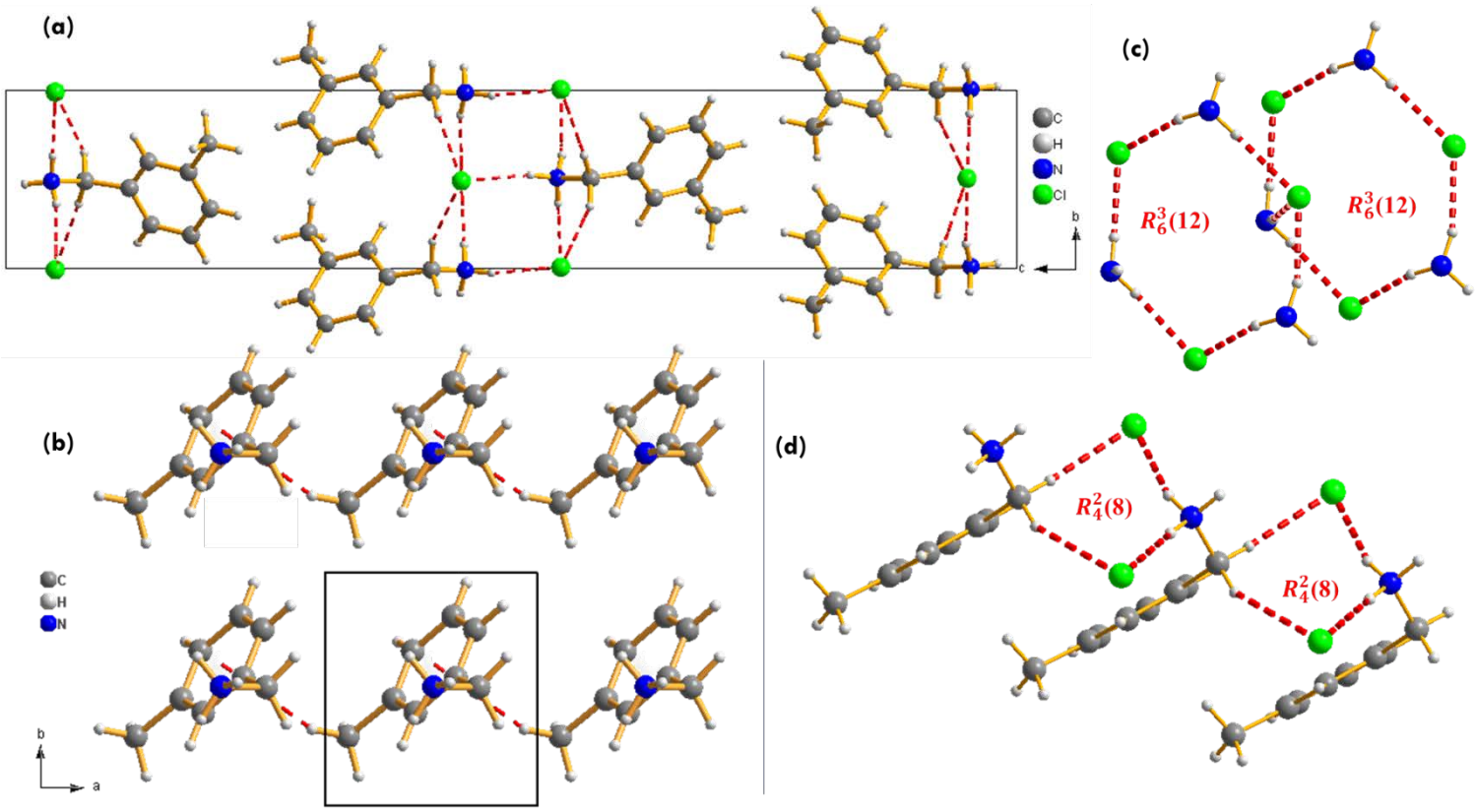

Fig. 4. The packing of compound (2) viewed along the *bc* plane **(a)**,**(b)** represents a view highlighting intermolecular interactions between organic cations C-H…π stacking and **(c,d)** the $R_6^3(12)$ and $R_4^2(8)$ motifs.

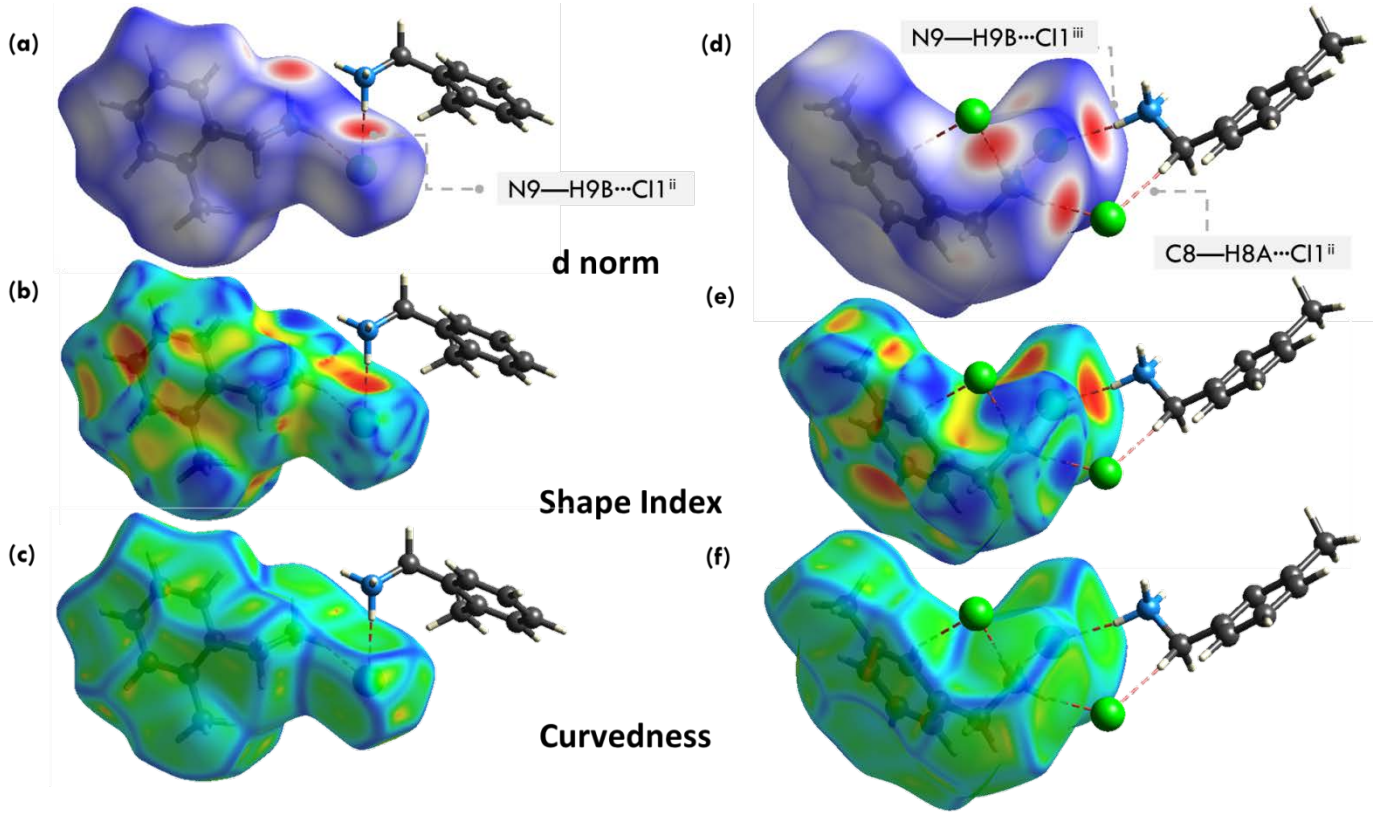

Fig. 5. Hirshfeld surfaces mapped with d_{norm} (-0,459 -0,938) (a) (dotted lines "red" represent hydrogen bonds), shape index (-1 - 1) (b) and curvedness (-4 - 0.4) (c) for compound (1), while (d,e,f) represents d_{norm} cartography (-0,515 - 1,196), shape index (-1 -1) and curvedness (-4 – 0.4) of compound (2), respectively.

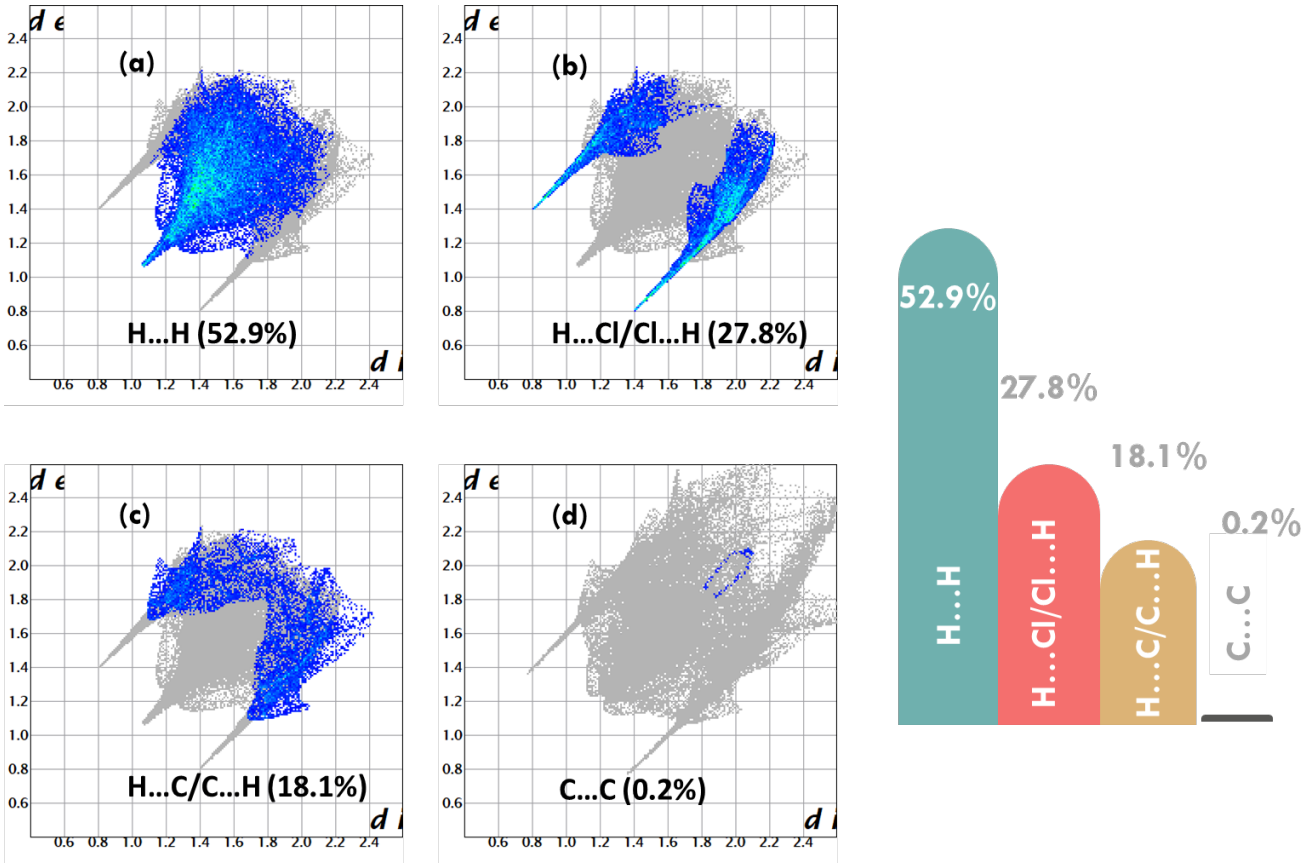

Fig. 6. 2D fingerprint plots of the main intercontacts of compound (1) showing the percentage of various intermolecular contacts contributed to the Hirshfeld surface.

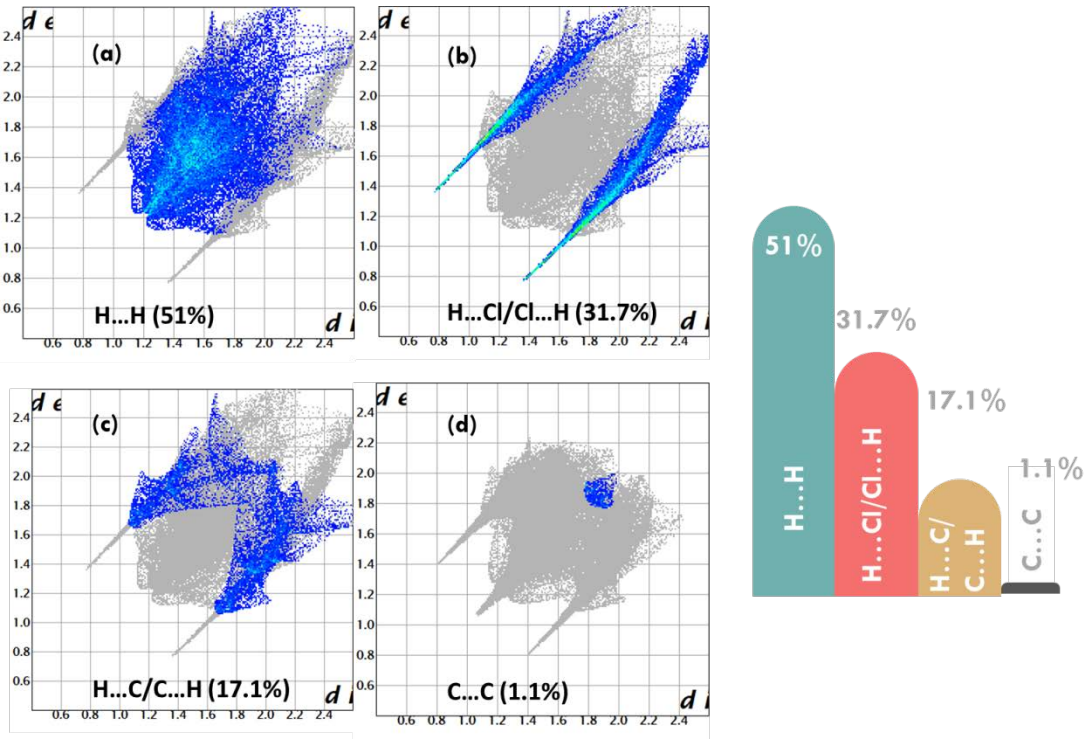

Fig. 7. 2D fingerprint plots of the main intercontacts of compound (2) showing the percentage of various intermolecular contacts contributed to the Hirshfeld surface.

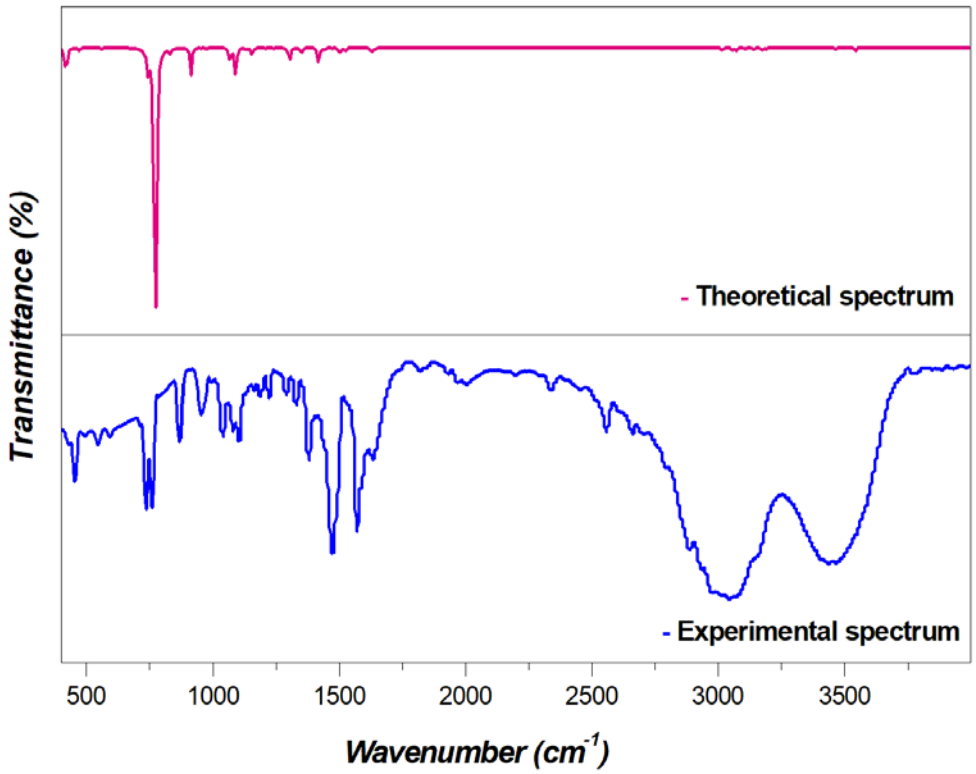

Fig. 8. Theoretical and experimental IR spectrum of compound (1).

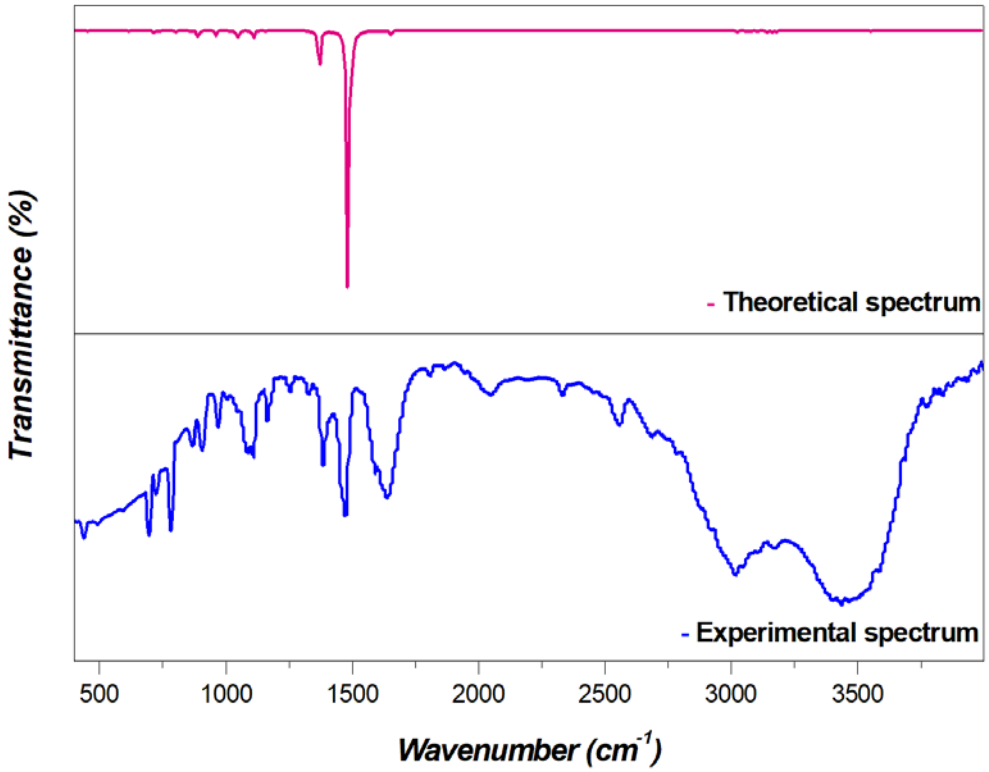

Fig. 9. Theoretical and experimental IR spectrum of compound (2).

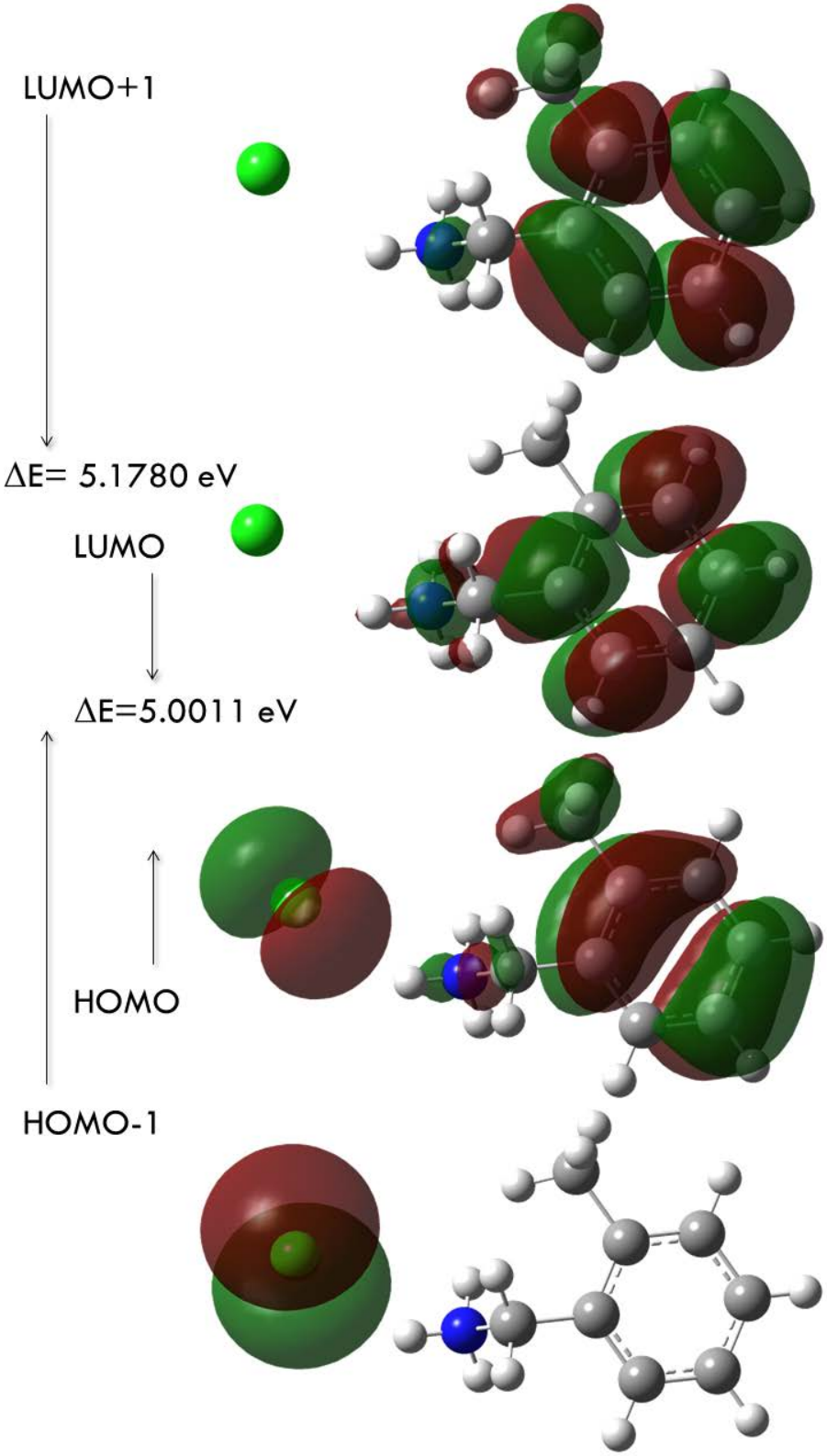

Fig. 10. Frontier molecular orbital plots of compound (1) computed with TD-DFT (B3LYP)/ 6-311++G(d,p) method.

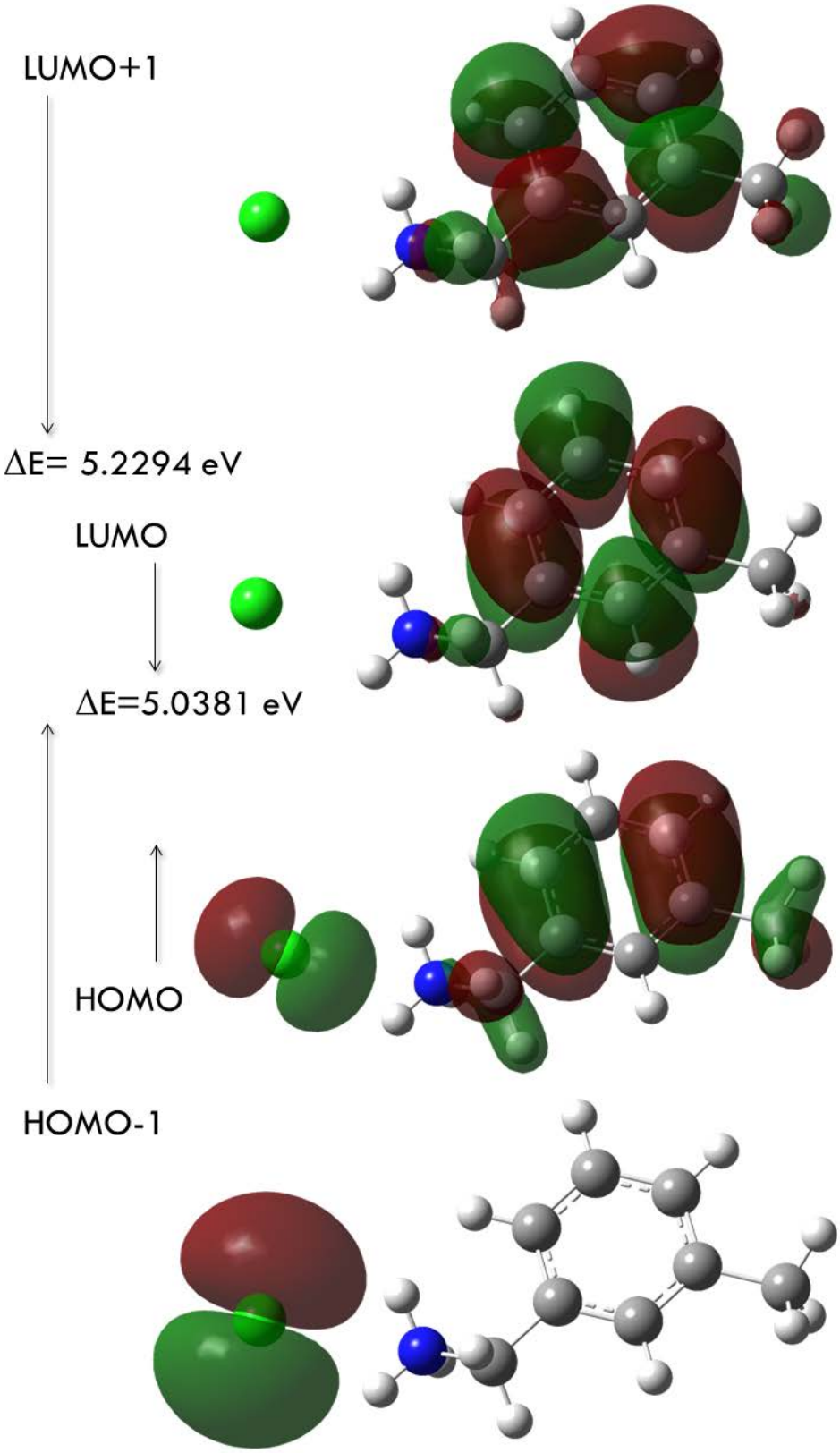

Fig. 11. Frontier molecular orbital plots of compound (2) computed with TD-DFT (B3LYP)/ 6-311++ G(d,p) method.

Table captions

Table 1. Experimental details of compounds (1) and (2).

Table 2. Selected bond distances (Å) and angles (°) for compounds (1) and (2) by X-ray data (with estimated standard deviation in parentheses) and by theoretical calculations.

Table 3. Hydrogen-bonds details (Å, °) of compounds (1) and (2).

Table 4. Enrichment ratio (ER) for compounds (1) and (2) and the percentage of each atom on the Hirshfeld surface.

Table 5. Observed and calculated wavenumbers (cm^{-1}) and assignments for compound (1).

Table 6. Observed and calculated wavenumbers (cm^{-1}) and assignments for compound (2).

Table 7. Global reactivity descriptors and calculated frontier molecular orbital parameters of compound (1) using TD-DFT(B3LYP)/6-311 ++ G(d,p) method.

Table 8. Global reactivity descriptors and calculated frontier molecular orbital parameters of compound (2) using TD-DFT(B3LYP)/6-311 ++ G(d,p) method.

Table 1. Experimental details of compounds (1) and (2).

Crystal data	Compound (1)	Compound (2)
N° CCDC	2096331	2096332
Chemical formula	$C_8H_{12}NCl$	$C_8H_{12}NCl$
Formula weight (g mol^{-1})	157.64	157.64
Crystal system, space group	Orthorhombic, $P2_12_12_1$	Orthorhombic, $P2_12_12_1$
Temperature (K)	150	150
a (Å)	4.7193 (6)	5.007 (4)
b (Å)	6.0599 (8)	5.501 (3)
c (Å)	28.242 (3)	31.384 (18)
V ($Å^3$)	807.68 (18)	864.5 (10)
Z	4	4
F(000)	336	336
μ (Mo *K*α)	0.40 mm^{-1}	0.37 mm^{-1}
Index ranges	$-6 \leq h \leq 3$, $-7 \leq k \leq 3$, $-36 \leq l \leq 20$	$-3 \leq h \leq 6$, $-6 \leq k \leq 6$, $-39 \leq l \leq 38$
Reflections collected	3361	3159
Independent reflections	1753	1651
Reflections with $I > 2\sigma(I)$	1647	1404
R_{int}	0.020	0.039
$(\sin\theta/\lambda)_{max}$ ($Å^{-1}$)	0.651	0.625
Absorption correction: multi-scan	T_{min}= 0.842, T_{max} = 0.957	T_{min}= 0.676, T_{max} = 0.953
Refined parameters	101	45
$R[F^2 > 2\sigma(F^2)]$	0.032	0.141
$wR(F^2)$	0.071	0.351
Goodness of fit	1.05	1.09
Flack parameter	0.04 (4)	0.51 (15)
$\Delta\rho_{max}$, $\Delta\rho_{min}$ (e $Å^{-3}$)	0.27, −0.18	0.87,−1.38

Table 2. Selected bond distances (Å) and angles (°) for compounds (1) and (2) by X-ray data (with estimated standard deviation in parentheses) and by theoretical calculations.

Bond length (Å)			**Bond angles (°)**		
	Calculated B3LYP 6-311++G(d.p)	X-Ray		Calculated B3LYP 6-311++G(d.p)	X-Ray
Compound (1)					
C1—C2	1.509	1.494 (4)	C3—C2—C7	117.82	117.7 (2)
C2—C3	1.40	1.394 (3)	C3—C2—C1	119.719	120.4 (2)
C3—C4	1.391	1.378 (3)	C7—C2—C1	122.46	121.9 (2)
C4—C5	1.392	1.379 (3)	C4—C3—C2	121.963	121.9 (2)
C5—C6	1.390	1.385 (3)	C5—C4—C3	119.908	120.1 (2)
C6—C7	1.40	1.388 (3)	C4—C5—C6	119.027	119.2 (2)
C7—C8	1.511	1.510 (3)	C5—C6—C7	121.377	121.3 (2)
C2—C7	1.409	1.406 (3)	C6—C7—C2	119.987	119.8 (2)
C8—N9	1.503	1.490 (3)	C6—C7—C8	117.789	119.5 (2)
			C2—C7—C8	122.311	120.7 (2)
			N9—C8—C7	111.434	112.35 (18)
Compound (2)					
C1—C2	1.509	1.518 (17)	C3—C2—C7	118.158	120.0
C2—C3	1.40	1.3900	C3—C2—C1	120.71	120.7 (10)
C3—C4	1.391	1.3900	C7—C2—C1	121.12	119.2 (10)
C4—C5	1.394	1.3900	C4—C3—C2	120.79	120.0
C5—C6	1.397	1.3900	C5—C4—C3	120.247	120.0
C6—C7	1.399	1.3900	C4—C5—C6	120.26	120.0
C6—C8	1.512	1.490 (15)	C7—C6—C5	118.867	120.0
C2—C7	1.397	1.3900	C7—C6—C8	120.439	123.3 (9)
C8—N9	1.485	1.492 (17)	C5—C6—C8	120.676	116.6 (9)
			C6—C7—C2	121.806	120.0
			C6—C8—N9	114.219	112.9 (11)

Table 3. Hydrogen-bonds details (Å, °) of compounds (1) and (2).

D—H···*A*	*D*—H(Å)	H···*A*(Å)	*D*···*A*(Å)	*D*—H···*A*(°)
Compound (1)				
N9—H9*A*···Cl1^{i}	0.91 (3)	2.40 (3)	3.222 (2)	151 (2)
N9—H9*B*···Cl1^{ii}	0.80 (3)	2.41 (3)	3.188 (2)	165 (3)
N9—H9*C*···Cl1	0.92 (2)	2.26 (3)	3.151 (2)	163 (2)
C1—H1*B*…Cg^{iii}	0.98	2.75	3.636	150
Compound (2)				
N9—H9*A*···Cl1	0.91	2.27	3.151 (14)	164
N9—H9*B*···Cl1^{i}	0.91	2.23	3.119 (11)	166
N9—H9*C*···Cl1^{ii}	0.91	2.27	3.175 (14)	178
C8—H8*B*···Cl1^{iii}	0.99	2.83	3.757 (18)	156
C8—H8*A*···Cl1^{iv}	0.99	2.77	3.756 (18)	176
C1—H1*B*…Cg^{v}	0.98	2.71	3.621	154

Symmetry codes for (1): (i) −*x*+1, *y*+1/2, −*z*+1/2; (ii) −*x*+1, *y*−1/2, −*z*+1/2;(iii) –*x*+3, *y*+5/2, -*z*+1/2.
Symmetry codes for (2): (i) x+1/2, −y+3/2, −z+1; (ii) x, y−1, z ;(iii) x+1, y−1, z; (iv) x+1, y, z; (v) *x*-2, *y*, *z*.
Cg : the centroid of the benzene ring.

Table 4. Enrichment ratio (ER) for compounds (1) and (2) and the percentage of each atom on the Hirshfeld surface.

(1)			
Enrichment	H	C	Cl
H	0.91	1.17	1.31
C		1.06	
Cl			
% surface	75.85	10.15	13.9
(2)			
Enrichment	H	C	Cl
H	0.89	1.29	1.32
C		0.26	
Cl			
% surface	75.4	8.75	15.85

Table 5. Observed and calculated wavenumbers (cm^{-1}) and assignments for compound (1).

	Calculated frequencies			
Exp.	Unscaled	Scaled	I^i	Vibrational assignments (% PED)
3435	3542	3393	28.99	υNH (99)
3423	3465	3319	11.36	υNH (100)
3054	3191	3057	14.18	υCH (90)
3044	3178	3044	16.24	υCH (97)
	3165	3032	2.28	υCH (94)
	3142	3010	13.37	υCH (94)
	3122	2991	2.02	υCH (98)
	3108	2977	16.13	υCH (96)
3015	3072	2943	21.12	υCH (97)
3015	3059	2930	23.52	υCH (100)
2878	3018	2891	23.08	υCH (100)
1634	1644	1616	12.56	υCC (67)
1634	1628	1600	50.61	βHNC (12) βHNH (64)
1571	1616	1588	0.90	υCC (35) βCCC (23)
	1527	1501	19.74	βHCC (31)
	1519	1493	11.22	βHCH (41)
	1503	1477	31.03	βHCH (47)
	1495	1470	7.09	βHCH (65) δHCCC (15)
1474	1487	1462	4.63	βHNH (34) βClHN (11)
	1473	1448	2.41	βHCC (40)
1474	1442	1417	17.36	βHNH (11) βClHN (13) δHNHC (32) γClCNH (10)
	1428	1404	6.69	βHCH (82)
1380	1418	1394	114.80	βHCH (31) δHCHN (46)
1329	1349	1326	47.73	υCC (10) βHCH (15) δHCHN (10)
1329	1318	1296	0.20	υCC (33) βHCC(30)
	1301	1279	124.90	βHNC (16) βHCH (14)
1290	1240	1219	5.87	υCC (38) βHCC(10)
1222	1207	1186	4.77	υCC (51)
1187	1188	1168	0.45	υCC (10) βHCC(72)
	1154	1134	60.28	βHCC (10) δHCHN (10)
1103	1133	1114	16.07	βNCC (11) δHNHC (41)
1081	1090	1071	213.82	υCC (21)
1039	1067	1049	112.85	υCC (43)
	1065	1047	7.41	βHCH (23)δHCCC (58) γCCCC (10)
	1016	999	2.66	υCC (11) βCCC (14) δHCCC (41)
	999	982	0.18	δHCCC (77) δCCCC (16)
952	971	954	12.06	υNC (64)
952	955	939	2.58	υNC (12) δHCCC (71)
	912	896	192.78	βHNC (13) βHCH (17) δHCHN (11)
	880	865	0.51	δHCCC (92)
869	832	818	34.47	υCC (34) βCCC (22)
761	778	765	1123,11	υNH (20) δHCCC (11)
738	772	759	1795,65	υNH (34) βClHN(10) δHCCC (10)
	746	733	207.16	δHCCC (24) δCCCC (11)
	728	716	24.74	βCCC (14) δCCCC (12)
547	605	595	1.86	βCCC (19) βNCC (12) δCCCC (12)

547	561	551	10.34	βCCC (10) δCCCC (15) γCCCC (11)
547	505	496	2.87	βCCC (11)
456	470	462	23.73	δCCCC (13) γCCCC (27)
456	420	413	241.67	υNH (18) υClH (53)
	409	402	6.92	βCCC (65)
	375	369	57.53	υClH (18) βHNH (14) δHNHC (15) γClCNH (19)
	326	320	13.29	βNCC (24) δCCCC (17)
	309	304	1.19	βCCC (76)
	208	204	2.50	δCCCC (30) γCCCC (32)
	162	159	0.75	δHCCC (71) γCCCC (15)
	125	123	6.24	δCCCC (36) γCCCC (31)
	91	89	5.42	βClHN (20) δHNHC (24) δNCCCC (11)
	77	76	3.80	δNCCC (57)

I^i: infrared intensity ($km.mol^{-1}$). υ, β, δ and γ denote stretching, in-plane bending, torsion and out-of-plane bending modes, respectively.

PED: potential energy distribution.

Table 6. Observed and calculated wavenumbers (cm^{-1}) and assignments for compound (2).

	Calculated frequencies			
Exp.	Unscaled	Scaled	I^i	Vibrational assignments (% PED)
3435	3553	3404	11.01	υNH (100)
3429	3478	3332	3.03	υNH (100)
3018	3182	3048	15.55	υCH (95)
3018	3161	3028	15.98	υCH (91)
3018	3154	3021	1.29	υCH (87)
3018	3143	3011	14.93	υCH (99)
2920	3104	2974	14.25	υCH (95)
2920	3103	2973	7.11	υCH (99)
2920	3077	2948	15.35	υCH (99)
2920	3061	2932	15.36	υCH (100)
	3025	2898	25.44	υCH (98)
1638	1653	1625	58.10	βHNH (50) δHNHC (44)
1594	1646	1618	8.82	υCC (57) βHCC(17)
1594	1626	1598	4.34	υCC (41) βCCC (26) βHCC(13)
	1523	1497	19.96	βHCC (42) βHCH (12)
	1501	1475	61.24	βHCH (47) δHCCC (11) δHCHN (21)
	1501	1475	415.71	υClH (12) βHCH (46)
	1489	1464	8.17	βHCH (75) δHCCC (13)
1473	1482	1457	3501,84	υClH(51) βHCH (27) δHCHN (17)
1473	1459	1434	21.62	υCC (32) βHCC (17) βHCH (12)
1473	1416	1392	2.46	βHCH (94)
1473	1382	1358	1.00	βHCH (45) δHCHN (10) γClCNH (19)
	1368	1345	693.81	υClH (27) δHCHN (42)
1327	1346	1323	0.34	υCC (25) βHCC (62)
1327	1325	1302	1.41	υCC (47) βHCC(15)
1253	1268	1246	0.94	υCC (31) βHCC(13) βCCC (13)
1164	1197	1177	0.08	υCC (15) βHCC(72)

1164	1182	1162	3.31	υCC (17) υNH (11) βHCC(40)
	1154	1134	6.05	βHNH(18) βHCH (24) δHNHC (24)
1108	1114	1095	0.31	υCC (16) βCCC (10) βHCC (33)
	1109	1090	109.63	βHNH(33) δHNHC (42)
	1062	1044	5.10	βHCH(21) δHCCC (56)
969	1047	1029	42.44	υNC (21) βHNC(12) δHCHN (14)
969	1044	1026	60.49	υNC (28) βHNC (22)
	1019	1002	5.26	βCCC (25) δHCCC (21)
	1012	995	4.20	υCC (27) βCCC (26) δHCCC (21)
	991	974	0.18	δHCCC (71) δCCCC (12)
969	958	942	53.95	υNC (17) βHNC (14)
905	920	904	1.28	δHCCC (78)
905	899	884	8.01	δHCCC (59)
867	889	874	94.29	υNC (18) βHNC (18)
	862	847	12.22	δHCHN (31) γClCNH (41)
784	802	788	25.20	δHCCC (65) δCCCC (18)
725	738	725	14.59	υCC (22) βCCC(31)
697	716	704	21.48	δHCCC (14) δCCCC (44)
	616	605	5.95	βCCN (19) γCCCC (27)
	532	523	1.18	υCC (35) βCCC(36)
	520	511	0.37	βCCC (21) γCCCC (20)
440	451	443	8.31	δHCCC (15) δCCCC (55)
440	415	408	4.59	βCCC(64) δHCHN(16)
	370	364	5.89	βCCC (13) βHNH(40) δHNHC (30)
	344	338	75.33	υNH (42) βCCN (20) δCCCC (13)
	263	258	2.71	βCCC (67)
	211	207	8.69	δCCCC (80)
	183	180	121.52	υNH (40) δCCCC (38)
	88	86	34.82	υNH (35) βCCN (29) δCCCC (21)
	48	47	3.32	βHNC (78)

I^i: infrared intensity (km.mol^{-1}). υ, β, δ and γ denote stretching, in-plane bending, torsion and out-of-plane bending modes, respectively.

PED: potential energy distribution.

Table 7. Global reactivity descriptors and calculated frontier molecular orbital parameters of compound (1) using TD-DFT(B3LYP)/6-311 ++ G(d,p) method.

Energies (eV)		Ionization potential I	9.56450847
Frontier orbitals		Electron affinity A	4.56333913
E_{HOMO}	-9.56450847	Descriptors	
E_{LUMO}	-4.56333913	Global electrophilicity (ω)	9.97747047
$\|E_{HOMO}-E_{LUMO}\|$	5.00116934	Electronegativity (χ)	7.0639238
E_{HOMO-1}	-9.58382851	Global chemical potential (μ)	-7.0639238
E_{LUMO+1}	-4.40578556	Global hardness (η)	2.50058467
$\|E_{HOMO-1}-E_{LUMO+1}\|$	5.17804295	Global softness (S)	0.199953237

Table 8. Global reactivity descriptors and calculated frontier molecular orbital parameters of compound (2) using TD-DFT(B3LYP)/6-311 ++ G(d,p) method.

Energies (eV)		Ionization potential I	9.54872590
Frontier orbitals		Electron affinity A	4.51054916
E_{HOMO}	-9.54872590	Descriptors	
E_{LUMO}	-4.51054916	Global electrophilicity (ω)	9.80827119
$\|E_{HOMO}-E_{LUMO}\|$	5.03817674	Electronegativity (χ)	7.02963753
E_{HOMO-1}	-9.58192372	Global chemical potential (μ)	-7.02963753
E_{LUMO+1}	-4.35245136	Global hardness (η)	2.51908837
$\|E_{HOMO-1}-E_{LUMO+1}\|$	5.22947236	Global softness (S)	0.19848450